

# Application of the direct quadrature method of moments to polydisperse gas–solid fluidized beds

Rong Fan<sup>\*</sup>, Daniele L. Marchisio<sup>1</sup>, Rodney O. Fox

*Department of Chemical Engineering, Iowa State University, 2114 Sweeney Hall, Ames, IA 50010-2230, USA*

Received 10 June 2003; received in revised form 17 October 2003; accepted 21 October 2003

---

## Abstract

Most of today's computational fluid dynamics (CFD) calculations for gas–solid flows are carried out assuming that the solid phase is monodispersed, whereas it is well known that in many applications, it is characterized by a particle size distribution (PSD). In order to properly model the evolution of a polydisperse solid phase, the population balance equation (PBE) must be coupled to the continuity and momentum balance equations. In this work, the recently formulated direct quadrature method of moments (DQMOM) is implemented in a multi-fluid CFD code to simulate particle aggregation and breakage in a fluidized-bed (FB) reactor. DQMOM is implemented in the code by representing each node of the quadrature approximation as a distinct solid phase. Since in the multi-fluid model, each solid phase has its own momentum balance, the nodes of the DQMOM approximation are convected with their own velocities. This represents an important improvement with respect to the quadrature method of moments (QMOM) where the moments are tracked using an average solid velocity. Two different aggregation and breakage kernels are tested and the performance of the DQMOM approximation with different numbers of nodes are compared. These results show that the approach is very effective in modeling solid segregation and elutriation and in tracking the evolution of the PSD, even though it requires only a small number of scalars.

© 2003 Elsevier B.V. All rights reserved.

**Keywords:** DQMOM; Fluidized beds; Population balance; Aggregation; Breakage

---

## 1. Introduction

Fluidized-bed (FB) reactors are widely used in many unit operations in the chemical, petroleum, pharmaceutical, agricultural, food and biochemical industries. They are well known as excellent reactors for their superior rates of heat and mass transfer between the gas and the solid particles, and for the efficient mixing of reacting species. With the development of high-speed computers, computational fluid dynamics (CFD) has played an important role in understanding the flow behavior of these two-phase flow systems. As is well known, most of today's CFD calculations for gas–solid flows are based on the assumption of a monodispersed solid phase (e.g., all particles have the same characteristic size) or on the assumption of a constant

particle size distribution (PSD) [1] (e.g. particles may be represented by a few different size classes but no changes in the PSD are accounted for). However, in many practical cases, solid particles belong to a PSD, which changes continuously according to the operating conditions. For example, in FB poly-olefin reactors, small catalyst particles (e.g., 20–80  $\mu\text{m}$ ) are introduced at a point above the gas distributor, and when exposed to the gas flow containing the monomer, polymerization occurs. At the early stage of polymerization, the catalyst particles fragment into a large number of small particles, which are quickly encapsulated by the newly formed polymer and grow continuously, reaching a typical size of 200–3000  $\mu\text{m}$ . Due to the differences in the polymer particle sizes, segregation occurs and fully grown polymer particles migrate to the bottom where they are removed from the reactor. The smaller pre-polymerized particles and fresh catalyst particles tend to migrate to the upper portions of the reactor and continue to react with monomers [2,3]. In addition, under certain undesirable operating conditions (e.g., when the reactor operates close to the polymer softening temperature), polymer particles can

---

<sup>\*</sup> Corresponding author. Tel.: +1-5152942079; fax: +1-5152942689.

E-mail address: rong@iastate.edu (R. Fan).

<sup>1</sup> Dipartimento di Scienza dei Materiali e Ingegneria Chimica, Politecnico di Torino, C.so Duca degli Abruzzi 24, 10129 Torino, Italy.



become “sticky” and during collisions can form large agglomerates that can possibly undergo sintering and cause defluidization. In the opposite situation, if the bed is too cold, the particles can become brittle and may fracture forming small fragments that elutriate with the gas [3,4]. Successful CFD models for FB poly-olefin reactors must be capable of describing such events in order to guide reactor design, scale up and optimization.

Recent research efforts have been directed towards the investigation of the effect of the PSD on the fluid dynamics of FB reactors. However, most work has focused on the segregation of binary mixtures. van Wachem et al. [5], using kinetic theory applied to a bimodal particle mixture, predicted the expansion of the bed with respect to a monodisperse PSD. Howley and Glasser [6] examined a general continuum model for a multi-particle fluidized bed and provided a description of the observed phenomenon of “layer inversion” for a binary mixture. In the work of Hoomans et al. [7], discrete particle simulations were used to investigate segregation phenomena in binary and ternary mixtures, good agreement is obtained in comparison to experiments.

In order to rigorously account for particle-related phenomena (e.g., agglomeration and breakage), the population balance equation (PBE) must be solved along with the continuity and momentum balance equations. However, attempts to incorporate the PBE into multi-fluid codes and to describe the evolution of the PSD in a FB reactor are very few. Recently, researchers have tried to couple the PBE with an Euler–Euler two-fluid model to simulate bubble-column reactors [8]. In their work, the dispersed phase was represented by 10 different size groups but only the momentum balance for the mixture was solved due to the significant reduction in the computing time. Thus, the 10 different classes were convected in the computational domain with the same mean algebraic velocity. Results showed good agreement with experiments for some hydrodynamic variables, but underestimated the global hold up [9]. Other researchers have also tried to solve the PBE with the multi-fluid code simultaneously, but most work was done in gas–liquid systems, not in gas–solid systems [10–12].

For spatially homogeneous systems, many different methods exist for solving the PBE and a lucid description of the mathematical and numerical issues involved can be found in Ref. [13]. The most direct method is the discretized population balance (DPB) approach or classes method (CM), in which the internal coordinate (e.g., particle length or volume) is discretized into a finite series of bins. In order to get reasonable results, a large number of classes must be used (e.g., 20–30), so that the DPB method is not a feasible approach for CFD calculations. An alternative approach uses Monte-Carlo simulations. This approach is based on the solution of the PBE in terms of its stochastic equivalent. A population of particles undergoes the “real” physical processes, and events occur according to the appropriate probabilities. For more details

on this approach, see Refs. [14,15]. Although this approach is theoretically applicable, especially for Lagrangian–Eulerian simulations, in order to reduce the statistical error, a very large number of particles must be used. Due to limitations on the computational resources, the full incorporation of Monte-Carlo methods with CFD codes is at the moment intractable [16,17].

An attractive alternative is represented by the method of moments (MOM) where the PSD is tracked through its moments by integrating out the internal coordinate. The main advantage of MOM is that the number of scalars required is very small (i.e., usually 4–6), which makes the implementation in CFD codes feasible. However, due to the difficulties related with expressing transport equations in terms of the moments themselves, the method has been scarcely applied. This is the so-called closure problem, pointed out first by Hulburt and Katz [18], and recently reviewed by Diemer and Olson [19]. As an alternative, McGraw [20] developed the so-called quadrature method of moments (QMOM), which is based on the approximation of the unclosed terms by using an ad-hoc quadrature formula. The quadrature approximation (i.e., its abscissas and weights) can be determined from the lower-order moments [21] by resorting to the product-difference (PD) algorithm [22]. QMOM has been extensively validated for several problems with different internal coordinates [23–25]. One of the main limitations of QMOM is that since the solid phase is represented through the moments of the distribution, the phase-average velocity of the different solid phases must be used to solve the transport equations for the moments. Thus, in order to use this method in the context of the multiphase flows, it is necessary to extend QMOM to handle cases where each particle size is convected by its own velocity.

In order to address these issues, the direct quadrature method of moments (DQMOM) has been formulated and validated [26]. DQMOM is based on the direct solution of the transport equations for weights and abscissas of the quadrature approximation. The calculation of the quadrature approximation through this direct formulation presents the advantage of being directly applicable to multi-variate PBE (i.e., PBE with more than one internal coordinate). Moreover, as it will become clear below, each node of the quadrature approximation can be treated as a distinct solid phase. DQMOM thus offers a powerful approach for describing polydisperse solids undergoing segregation, growth, aggregation and breakage processes in the context of CFD simulations.

In this work, DQMOM is implemented in a multi-fluid model for simulating polydisperse gas–solid FB reactors. First, the general governing equations for the multi-fluid model are presented in Section 2. Next, in Section 3, the implementation of aggregation and breakage in the DQMOM multi-fluid model is described. Finally, CFD predictions for the evolution of the PSD in a FB reactor with aggregation and breakage are presented in Section 4. Conclusions are drawn in Section 5.



## 2. The DQMOM-multi-fluid model

The detailed mathematical modeling of FB reactors is very complex since it involves interactions between closely coupled phenomena, such as multiphase flow dynamics, mass transfer, heat transfer, chemical reactions, and particulate processes such as aggregation and breakage. The simultaneous numerical solution of the equations for continuity, momentum, energy, and chemical species is required. In addition, for polydisperse solids, a PBE is needed. For simplicity, in this work, the FB is assumed to be isothermal with no chemical reactions, and the PSD changes only due to aggregation and breakage. Thus, our goal is to build the link between the PBE and the continuity and momentum balance equations, and to obtain an economical but accurate method for describing the time evolution of the PSD and the gas and solids flows fields. In what follows, the multi-fluid model for gas–solid FB reactors is first described briefly. More details can be found elsewhere [27]. The implementation of DQMOM in the multi-fluid model is then described in some detail.

### 2.1. Multi-fluid model for gas–solid flow

The multi-fluid model is an extension of the two fluid model for gas–solid flows [27]. In this model, the gas and solid phases are treated as inter-penetrating continua in an Eulerian framework. The gas phase is considered as the primary phase, whereas the solid phases are considered as secondary or dispersed phases. Each solid phase is characterized by a specific diameter, density and other properties. The primary and dispersed phases are characterized by volume fractions, and by definition, the volume fractions of all phases must sum to unity:

$$\varepsilon_g + \sum_{\alpha=1}^N \varepsilon_{s\alpha} = 1, \quad (1)$$

where  $\varepsilon_g$  is the gas volume fraction,  $\varepsilon_{s\alpha}$  is the volume fraction of  $\alpha^{\text{th}}$  solid phase, and  $N$  is the total number of solid phases.

The continuity equation for the gas phase is

$$\frac{\partial \varepsilon_g \rho_g}{\partial t} + \nabla \cdot (\varepsilon_g \rho_g \mathbf{u}_g) = 0, \quad (2)$$

where  $\rho_g$  is the density of the gas, and  $\mathbf{u}_g$  is the gas velocity. In the absence of aggregation and breakage, the continuity equation of the  $\alpha^{\text{th}}$  solid phase is

$$\frac{\partial \varepsilon_{s\alpha} \rho_{s\alpha}}{\partial t} + \nabla \cdot (\varepsilon_{s\alpha} \rho_{s\alpha} \mathbf{u}_{s\alpha}) = 0, \quad (3)$$

where  $\rho_{s\alpha}$  is the density of the  $\alpha^{\text{th}}$  solid phase and  $\mathbf{u}_{s\alpha}$  is the velocity of the  $\alpha^{\text{th}}$  solid phase. As will be shown below, aggregation and breakage processes will result in additional terms on the right-hand side of Eq. (3).

The momentum balance for the gas phase is

$$\frac{\partial}{\partial t} (\varepsilon_g \rho_g \mathbf{u}_g) + \nabla \cdot (\varepsilon_g \rho_g \mathbf{u}_g \mathbf{u}_g) = \nabla \cdot \mathbf{S}_g + \sum_{\alpha=1}^N \mathbf{f}_{g\alpha} + \varepsilon_g \rho_g \mathbf{g}. \quad (4)$$

Likewise, for the solid phases, the momentum balances are

$$\begin{aligned} \frac{\partial}{\partial t} (\varepsilon_{s\alpha} \rho_{s\alpha} \mathbf{u}_{s\alpha}) + \nabla \cdot (\varepsilon_{s\alpha} \rho_{s\alpha} \mathbf{u}_{s\alpha} \mathbf{u}_{s\alpha}) \\ = \nabla \cdot \mathbf{S}_{s\alpha} - \mathbf{f}_{g\alpha} + \sum_{l=1}^N \mathbf{f}_{l\alpha} + \varepsilon_{s\alpha} \rho_{s\alpha} \mathbf{g}, \end{aligned} \quad (5)$$

where  $\mathbf{S}_g$  and  $\mathbf{S}_{s\alpha}$  are the stress tensors for the gas and the solid phases, respectively, and  $\mathbf{g}$  is the gravity vector. The interaction force between the gas phase and the  $\alpha^{\text{th}}$  solid phase is denoted by  $\mathbf{f}_{g\alpha}$ , whereas the interaction force between the  $\alpha^{\text{th}}$  solid phase and the  $l^{\text{th}}$  solid phase is denoted by  $\mathbf{f}_{l\alpha}$ .

A simple Newtonian closure is used for the gas-phase stress tensor. Two entirely different methods are used to calculate the solid stress tensor in different regimes. For the plastic or slowly shearing regime, theories from the study of soil mechanics are used. For the viscous or rapidly shearing regime, kinetic theory is used [27–29]. The constitutive relations for the gas and solids stress tensors are summarized in Table 1. Studies on the dynamics of a single particle in a fluid have shown that many forces contribute to the gas–solid interactions [30], but in this work, only the drag force and the buoyancy force are accounted for. The drag correlation used was derived by Gidaspow [28]. The interaction forces between the different solid phases are expressed in terms of the drag force and the enduring contact force in the plastic regime, as described by Syamlal [27]. The gas–solid and solid–solid interaction forces are listed in Table 2. A detailed discussion of the parameters in the multi-fluid model can be found elsewhere [27]. The reader should keep in mind that the solid stress tensor and drag formulation appearing in Tables 1 and 2 are slight modifications of the corresponding monodisperse solids models. Thus, the simulation results found using other polydisperse models (e.g., Refs. [1,31]) may differ quantitatively from those reported here.

### 2.2. Direct quadrature method of moments

A polydisperse solid phase can be modeled by a multivariate distribution function  $n(L, \mathbf{u}_s)$  for the characteristic particle size  $L$  and the particle velocity vector  $\mathbf{u}_s$  whose transport equation is [26]

$$\begin{aligned} \frac{\partial n(L, \mathbf{u}_s; \mathbf{x}, t)}{\partial t} + \nabla \cdot [\mathbf{u}_s n(L, \mathbf{u}_s; \mathbf{x}, t)] + \nabla_{\mathbf{u}_s} \cdot [\mathbf{F} n(L, \mathbf{u}_s; \mathbf{x}, t)] \\ = S(L, \mathbf{u}_s; \mathbf{x}, t), \end{aligned} \quad (6)$$



Table 1

Constitutive relations for gas and solids stress tensors, and the solids collision parameters [27]

*Gas stress tensor*

$$\begin{aligned} \mathbf{S}_g &= -P_g \mathbf{I} + \tau_g \\ \tau_g &= 2\epsilon_g \mu_g \mathbf{D}_g - 2/3 \epsilon_g \mu_g \text{Tr}(\mathbf{D}_g) \mathbf{I} \\ \mathbf{D}_g &= 1/2 [\nabla \mathbf{u}_g + (\nabla \mathbf{u}_g)^T] \end{aligned}$$

*Solids stress tensor (viscous regime)*

$$\begin{aligned} \mathbf{S}_{sz}^v &= -P_{sz}^v \mathbf{I} + \tau_{sz}^v \\ P_{sz}^v &= K_{1z} \epsilon_{sz}^2 \theta_z \\ \tau_{sz}^v &= 2\mu_{sz}^v \mathbf{D}_{sz} + \lambda_{sz}^v \text{Tr}(\mathbf{D}_{sz}) \mathbf{I} \\ \theta_z &= \left( \frac{-K_{1z} \epsilon_{sz} \text{Tr}(\mathbf{D}_{sz}) + \sqrt{K_{1z}^2 \text{Tr}^2(\mathbf{D}_{sz}) \epsilon_{sz}^2 + 4K_{4z} \epsilon_{sz} [K_{2z} \text{Tr}^2(\mathbf{D}_{sz}) + 2K_{3z} \text{Tr}(\mathbf{D}_{sz}^2)]}}{2\epsilon_{sz} K_{4z}} \right)^2 \end{aligned}$$

$$\lambda_{sz}^v = K_{2z} \epsilon_{sz} \theta_z^{1/2}$$

$$\mu_{sz}^v = K_{3z} \epsilon_{sz} \theta_z^{1/2}$$

$$K_{1z} = 2(1+e)\rho_{sz} g_z$$

$$K_{2z} = 4d_{pz} \rho_{sz} (1+e) \frac{\epsilon_{sz} g_z}{3\pi^{1/2}} - \frac{2}{3} K_{3z}$$

$$K_{3z} = \frac{d_{pz} \rho_{sz}}{2} \left[ \frac{\pi^{1/2}}{3(3-e)} [1 + 0.4(1+e)(3e-1)\epsilon_{sz} g_z] + \frac{8\epsilon_{sz} g_z (1+e)}{5\pi^{1/2}} \right]$$

$$K_{4z} = \frac{12(1-e^2)\rho_{sz} g_z}{d_{pz} \pi^{1/2}}$$

$$g_z = \frac{1}{\epsilon_g} + \frac{3d_{pz}}{2\epsilon_g^2} \sum_{j=1}^N \frac{\epsilon_{sj}}{d_{pj}}$$

$$\mathbf{D}_{sz} = 1/2 [\nabla \mathbf{u}_{sz} + (\nabla \mathbf{u}_{sz})^T]$$

*Solids collision parameters*

$$g_{xj} = \frac{1}{\epsilon_g} + \frac{3d_{pz} d_{pj}}{\epsilon_g^2 (d_{pz} + d_{pj})} \sum_{\lambda=1}^N \frac{\epsilon_{s\lambda}}{d_{p\lambda}}$$

$$\sigma_{xj} = (d_z + d_j)/2$$

$$\theta_s = \frac{\epsilon_{sz} \rho_{sz} \theta_z + \epsilon_{sj} \rho_{sj} \theta_j}{\epsilon_{sz} \rho_{sz} + \epsilon_{sj} \rho_{sj}} (m_z + m_j)$$

$$m_z = \pi/6 d_{pz}^3 \rho_{sz}$$

To be consistent with the notation used in MFIX, the abscissa  $L_z$  and  $d_{pz}$  are equivalent, and represent the particle size for the  $\alpha^{\text{th}}$  solid phase.

where  $\mathbf{x}$  is the spatial coordinate, and  $t$  is time. In this expression,  $S(L, \mathbf{u}_s; \mathbf{x}, t)$  is a “source” term that represents discontinuous jumps in property space (i.e., due to aggregation and breakage events), whereas  $\mathbf{F}$  is the force acting to accelerate the particles. Note that when Eq. (6) is used to evaluate the size-conditioned average velocity of a particle  $\mathbf{u}_{s\alpha} = \langle \mathbf{u}_s | L = L_\alpha \rangle$ , the size-conditioned average force  $\langle \mathbf{F} | L = L_\alpha \rangle$  must be consistent with the terms on the right-hand side of Eq. (5). In this work, we will circumvent the difficulty of finding a consistent definition for  $\mathbf{F}$  by simply using Eq. (5) to define  $\mathbf{u}_{s\alpha}$ .

Using DQMOM, the distribution function  $n(L, \mathbf{u}_s)$  is approximated by a summation of  $N$  Dirac delta functions:

$$n(L, \mathbf{u}_s; \mathbf{x}, t) = \sum_{\alpha=1}^N \omega_\alpha(\mathbf{x}, t) \delta[L - L_\alpha(\mathbf{x}, t)] \delta[\mathbf{u}_s - \mathbf{u}_{s\alpha}(\mathbf{x}, t)], \quad (7)$$

where  $\omega_\alpha$  is the weight of the delta function centered at the characteristic particle size  $L_\alpha$  and the characteristic velocity  $\mathbf{u}_{s\alpha}$ . If Eq. (7) is inserted into Eq. (6), and a moment transformation is applied, it is possible to derive the transport equations for the  $N$  weights  $\omega_\alpha$  (zero-order moment) and the  $N$  abscissas  $L_\alpha$  (first-order moment with respect to length). As noted above, the conditional first-order moment of  $\mathbf{u}_s$  can be used to derive the momentum balances for the  $N$  velocities  $\mathbf{u}_{s\alpha}$ . However, since we will assume that Eq. (5) holds, the transport equations for the  $N$  weights  $\omega_\alpha$  and  $N$  abscissas  $L_\alpha$  can be found from the DQMOM representation of the PSD:

$$\begin{aligned} n(L; \mathbf{x}, t) &= \int_{-\infty}^{+\infty} n(L, \mathbf{u}_s; \mathbf{x}, t) d\mathbf{u}_s \\ &= \sum_{\alpha=1}^N \omega_\alpha(\mathbf{x}, t) \delta[L - L_\alpha(\mathbf{x}, t)]. \end{aligned} \quad (8)$$

Integrating out the velocity in Eq. (6), we obtain the solid-phase PBE:

$$\frac{\partial n(L; \mathbf{x}, t)}{\partial t} + \nabla \cdot [\langle \mathbf{u}_s | L \rangle n(L; \mathbf{x}, t)] = S(L; \mathbf{x}, t), \quad (9)$$

where  $\langle \mathbf{u}_s | L \rangle$  is the mean velocity conditioned on  $L$ :

$$\langle \mathbf{u}_s | L \rangle n(L; \mathbf{x}, t) = \int_{-\infty}^{+\infty} \mathbf{u}_s n(L, \mathbf{u}_s; \mathbf{x}, t) d\mathbf{u}_s, \quad (10)$$

and  $S(L; \mathbf{x}, t)$  is the size-dependent source term for aggregation and breakage. Notice that, by definition,  $\langle \mathbf{u}_s | L = L_\alpha \rangle = \mathbf{u}_{s\alpha}$ .

Table 2

Gas–solid and solid–solid interaction forces [27]

*Gas–solid interaction force*

$$\begin{aligned} \mathbf{f}_{gz} &= -\epsilon_{sz} \nabla P_g - F_{gz}(\mathbf{u}_{sz} - \mathbf{u}_g) \\ F_{gz} &= \begin{cases} 150 \frac{\epsilon_{sz}^2 \mu_g}{\epsilon_g d_{pz}^2} + 1.75 \frac{\epsilon_{sz} \rho_g |\mathbf{u}_g - \mathbf{u}_{sz}|}{d_{pz}} & \text{if } \epsilon_g \leq 0.8 \\ \frac{3}{4} C_D \frac{\epsilon_{sz} \rho_g \epsilon_g |\mathbf{u}_g - \mathbf{u}_{sz}|}{d_{pz}} \epsilon_g^{-2.65} & \text{if } \epsilon_g > 0.8 \end{cases} \end{aligned}$$

$$C_D = \begin{cases} \frac{24}{Re_{pz}} (1 + 0.15 Re_{pz}^{0.687}) & \text{if } Re_{pz} \leq 1000 \\ 0.44 & \text{if } Re_{pz} > 1000 \end{cases}$$

$$Re_{pz} = \frac{\epsilon_g \rho_g |\mathbf{u}_g - \mathbf{u}_{sz}| d_{pz}}{\mu_g}$$

*Solid–solid interaction force*

$$\begin{aligned} \mathbf{f}_{lz} &= - (F_{lz} + F')(\mathbf{u}_{sz} - \mathbf{u}_{sl}) \\ F_{lz} &= \frac{3(1 + e_{lz}) \left( \frac{\pi}{2} + \frac{C_{l\alpha} \pi^2}{8} \right) \epsilon_{sl} \rho_{sl} \epsilon_{sz} \rho_{sz} (d_{pl} + d_{pz})^2 g_z |\mathbf{u}_{sl} - \mathbf{u}_{sz}|}{2\pi(\rho_{sl} d_{pl}^3 + \rho_{sz} d_{pz}^3)} \end{aligned}$$

$$F' = \begin{cases} 2.0 \times 10^8 (\epsilon_g - \epsilon_g^*)^3 & \text{if } \epsilon_g \leq \epsilon_g^* \\ 0 & \text{if } \epsilon_g > \epsilon_g^* \end{cases}$$



Before explaining how to obtain transport equations for the weights  $\omega_\alpha$  and abscissas  $L_\alpha$ , it is important to highlight that previous validation studies of DQMOM and comparison of its performance with QMOM have demonstrated that by using as few as  $N=2$  or 3 nodes, the lower-order moments of the PSD:

$$m_k(\mathbf{x}, t) = \int_0^\infty n(L; \mathbf{x}, t) L^k dL \approx \sum_{\alpha=1}^N \omega_\alpha(\mathbf{x}, t) L_\alpha^k(\mathbf{x}, t), \quad (11)$$

are tracked with surprisingly small errors [24–26]. The DQMOM approach has been tested for predicting the time evolution of the PSD under aggregation, breakage and molecular growth [26]. The ability of the model to track the moments of the PSD does not give any physical meaning to the nodes of the quadrature approximation and, as explained in the original formulation of the model [20], the weights  $\omega_\alpha$  and abscissas  $L_\alpha$  are simply the quadrature approximation for the moments. However, it has been shown that the nodes can be thought of as different solid phases with characteristic particle size  $L_\alpha$  and velocity  $\mathbf{u}_{s\alpha}$ , and that the quadrature approximation actually resembles the shape of the underlying PSD [26]. It is thus clear that each node of the quadrature approximation is calculated in order to guarantee that the moments of the PSD are tracked with high accuracy but, at the same time, each node is treated as a distinct solid phase giving the DQMOM-multi-fluid model the ability to treat polydisperse solids.

The rigorous derivation of the transport equations for the weights  $\omega_\alpha$  and weighted abscissas  $\mathcal{L}_\alpha(\mathcal{L}_\alpha = L_\alpha \omega_\alpha)$  is reported in Ref. [26]. Here we limit our discussion to a brief review of the mathematical approach. The transport equations for the weights and weighted abscissas can be written as:

$$\begin{aligned} \frac{\partial \omega_\alpha}{\partial t} + \nabla \cdot (\mathbf{u}_{s\alpha} \omega_\alpha) &= a_\alpha, \\ \frac{\partial \mathcal{L}_\alpha}{\partial t} + \nabla \cdot (\mathbf{u}_{s\alpha} \mathcal{L}_\alpha) &= b_\alpha, \end{aligned} \quad (12)$$

where  $a_\alpha$  and  $b_\alpha$  are defined through a linear system found from the first  $2N$  moments (e.g.,  $k=0, \dots, 2N-1$ ) of the PSD. This linear system can be written in matrix form as:

$$\mathbf{A}\boldsymbol{\alpha} = \mathbf{d}, \quad (13)$$

where the  $2N \times 2N$  coefficient matrix  $\mathbf{A} = [\mathbf{A}_1 \mathbf{A}_2]$  is defined by

$$\mathbf{A}_1 = \begin{bmatrix} 1 & \dots & 1 \\ 0 & \dots & 0 \\ -L_1^2 & \dots & -L_N^2 \\ \vdots & \ddots & \vdots \\ 2(1-N)L_1^{2N-1} & \dots & 2(1-N)L_N^{2N-1} \end{bmatrix} \quad (14)$$

and

$$\mathbf{A}_2 = \begin{bmatrix} 0 & \dots & 0 \\ 1 & \dots & 1 \\ 2L_1 & \dots & 2L_N \\ \vdots & \ddots & \vdots \\ (2N-1)L_1^{2N-2} & \dots & (2N-1)L_N^{2N-2} \end{bmatrix} \quad (15)$$

The  $2N$  vector of unknowns  $\boldsymbol{\alpha}$  is defined by

$$\boldsymbol{\alpha} = [a_1 \dots a_N b_1 \dots b_N]^T = \begin{bmatrix} \mathbf{a} \\ \mathbf{b} \end{bmatrix}, \quad (16)$$

and the known right-hand side is

$$\mathbf{d} = [\bar{S}_0^{(N)} \dots \bar{S}_{2N-1}^{(N)}]^T. \quad (17)$$

The source term for the  $k^{\text{th}}$  moment  $\bar{S}_k^{(N)}$  is defined by

$$\bar{S}_k^{(N)}(\mathbf{x}, t) = \int_0^\infty L^k S(L; \mathbf{x}, t) dL. \quad (18)$$

As shown below, with the DQMOM approximation, the right-hand side of Eq. (18) is closed in terms of the  $N$  weights and abscissas. The superscript  $(N)$  on  $\bar{S}_k^{(N)}$  is a reminder that  $N$  nodes are used to approximate the integral. As  $N$  increases, the quadrature approximation will approach the exact value, albeit at a higher computational cost.

If the abscissas  $L_\alpha$  are unique, then  $\mathbf{A}$  will be full rank. For this case, the source terms for the transport equations of the weights  $\omega_\alpha$  and weighted lengths  $\mathcal{L}_\alpha$  can be found simply by inverting  $\mathbf{A}$  in Eq. (13):

$$\boldsymbol{\alpha} = \mathbf{A}^{-1} \mathbf{d}. \quad (19)$$

If at any point in the computational domain two abscissas are equal, then the matrix  $\mathbf{A}$  is not full rank (or the matrix is singular), and therefore, it is impossible to invert it. In order to overcome this problem, a small perturbation can be added to the abscissas to make  $\mathbf{A}$  full rank. However, this method does not work very well as the number of nodes increases, and alternative approaches can be used.

First of all, it is important to develop a reliable technique to detect any singularity of the matrix  $\mathbf{A}$ . The matrix can be singular (or nearly singular) when two abscissas become too close to each other with an increase in the number of nodes. In such situations, the inverse of the matrix can still be calculated, but it has a large error. Thus, a safe way to detect a singularity is to calculate the condition number of the matrix  $\mathbf{A}$  when  $N > 3$ . Here, the condition number is defined as the ratio between the largest and smallest singular values. The reciprocal of the condition number can be used as a control variable to monitor singularity of the matrix  $\mathbf{A}$ . If it is smaller than a small number (e.g.,  $1.0 \times 10^{-12}$ ), the matrix is considered singular.



When a singularity is detected, two possible approaches can be used to overcome the problem. In the first one, for the computational cells where singularity happens, the matrix  $\mathbf{A}$  is not inverted and the source vector  $\alpha$  is simply set to zero. In this case, convection in physical space will “solve” the singularity. If the second approach is used, the source vector  $\alpha$  is estimated from the average of the source vectors from neighboring cells. However, it is important to highlight that the frequency of this event is very low in the simulations. This result is also confirmed by the fact that the abscissas  $L_\alpha$  are equal to each other only if the final PSD is a monodispersed distribution centered at a unique value, which is not the case in most practical applications. It is also clear that this singularity problem of the matrix  $\mathbf{A}$  is more related to boundary or initial conditions where monodispersed distributions might be used.

In order to be consistent with the variables used in the multi-fluid model, we need to relate the weights and abscissas to the solid volume fraction  $\varepsilon_{sz}$  and the effective length  $\varepsilon_{sz}L_\alpha$  for each solid phase. The volume fraction of each solid phase is related to the abscissas  $L_\alpha$  and weights  $\omega_\alpha$  by

$$\varepsilon_{sz} = k_v L_\alpha^3 \omega_\alpha = k_v \frac{\mathcal{V}_\alpha^3}{\omega_\alpha^2}, \quad (20)$$

and the effective length of the solid phase is

$$\varepsilon_{sz}L_\alpha = k_v L_\alpha^4 \omega_\alpha = k_v \frac{\mathcal{V}_\alpha^4}{\omega_\alpha^3}, \quad (21)$$

where  $k_v$  is a volumetric shape factor (e.g., for spherical particles  $k_v = \pi/6$ ). Using Eqs. (20) and (21), the transport equations for  $\varepsilon_{sz}$  and  $L_\alpha$  can be written as

$$\begin{aligned} \frac{\partial \varepsilon_{sz} \rho_{sz}}{\partial t} + \nabla \cdot (\mathbf{u}_{sz} \varepsilon_{sz} \rho_{sz}) &= 3k_v \rho_{sz} L_\alpha^2 b_\alpha - 2k_v \rho_{sz} L_\alpha^3 a_\alpha, \\ \frac{\partial \varepsilon_{sz} L_\alpha \rho_{sz}}{\partial t} + \nabla \cdot (\mathbf{u}_{sz} \varepsilon_{sz} L_\alpha \rho_{sz}) &= 4k_v \rho_{sz} L_\alpha^3 b_\alpha - 3k_v \rho_{sz} L_\alpha^4 a_\alpha. \end{aligned} \quad (22)$$

The first equation represents the continuity equation for the  $\alpha^{\text{th}}$  solid phase in the presence of aggregation and breakage (cf. Eq. (3)). It is clear that because of aggregation and breakage, the volume fraction of each solid phase will change according to its characteristic length  $L_\alpha$  is order to mimic the evolution of the PSD. It is straightforward to verify that the summation of the transport equations over the  $N$  solid phases leads to a null source term. This implies that aggregation and breakage do not change the total solid volume fraction (i.e., the solid volume fraction is preserved). Thus, the source term for the gas volume fraction  $\varepsilon_g$  is null, and the relative volume fractions of the different solid phases change due to aggregation and breakage. The second equation in Eq. (22) is solved in the multi-fluid model as a set of user-defined scalars. Finally, note that using Eq. (20), the weights  $\omega_\alpha$  can be computed from  $\varepsilon_{sz}$  and

$L_\alpha$  whenever they are needed (e.g., to compute  $\mathbf{d}$ ) during the course of a simulation. Eqs. (5) and (22) constitute the DQMOM-multi-fluid model for a polydisperse solid phase. The only remaining task is to relate  $\mathbf{d}$  in Eq. (13) to the well-known expressions for aggregation and breakage from the theory of population balances [13].

### 3. Implementation of aggregation and breakage

In this work, we will consider changes in the PSD due only to aggregation and breakage. For this case, the moment transform of the aggregation and breakage source term is [24]

$$\bar{S}_k^{(N)}(\mathbf{x}, t) = \bar{B}_k^a(\mathbf{x}, t) - \bar{D}_k^a(\mathbf{x}, t) + \bar{B}_k^b(\mathbf{x}, t) - \bar{D}_k^b(\mathbf{x}, t), \quad (23)$$

where the moments of the birth and death rates are defined by

$$\bar{B}_k^a(\mathbf{x}, t) = \frac{1}{2} \int_0^\infty \int_0^\infty \beta(L, \lambda) (L^3 + \lambda^3)^{k/3} n(\lambda; \mathbf{x}, t) n(L; \mathbf{x}, t) d\lambda dL, \quad (24)$$

$$\bar{D}_k^a(\mathbf{x}, t) = \int_0^\infty \int_0^\infty L^k \beta(L, \lambda) n(\lambda; \mathbf{x}, t) n(L; \mathbf{x}, t) d\lambda dL \quad (25)$$

$$\bar{B}_k^b(\mathbf{x}, t) = \int_0^\infty \int_0^\infty L^k a(\lambda) b(L|\lambda) n(\lambda; \mathbf{x}, t) d\lambda dL \quad (26)$$

$$\bar{D}_k^b(\mathbf{x}, t) = \int_0^\infty L^k a(L) n(L; \mathbf{x}, t) dL. \quad (27)$$

In these expressions,  $\beta(L, \lambda)$  is the aggregation kernel, which is proportional to the frequency of collision of two particles with lengths  $L$  and  $\lambda$ ,  $a(L)$  is the breakage kernel, which is the frequency of disruption of a particle of length  $L$ , and  $b(L|\lambda)$  is the fragment distribution function, which contains information on the fragments produced by a breakage event.

DQMOM is based on the quadrature approximation reported in Eq. (8). Thus, using this approximation, the source term in Eq. (23) is closed:

$$\begin{aligned} \bar{S}_k^{(N)}(\mathbf{x}, t) &= \frac{1}{2} \sum_{\alpha=1}^N \sum_{\gamma=1}^N \omega_\alpha \omega_\gamma (L_\alpha^3 + L_\gamma^3)^{k/3} \beta_{\alpha\gamma} \\ &\quad - \sum_{\alpha=1}^N \sum_{\gamma=1}^N \omega_\alpha \omega_\gamma L_\alpha^k \beta_{\alpha\gamma} + \sum_{\alpha=1}^N \omega_\alpha a_\alpha^* \bar{b}_\alpha^{(k)} \\ &\quad - \sum_{\alpha=1}^N \omega_\alpha L_\alpha^k a_\alpha^*, \end{aligned} \quad (28)$$

where  $\beta_{\alpha\gamma} = \beta(L_\alpha, L_\gamma)$ ,  $a_\alpha^* = a(L_\alpha)$ , and

$$\bar{b}_\alpha^{(k)} = \int_0^{+\infty} L^k b(L|L_\alpha) dL. \quad (29)$$



As concerns the daughter distribution function, the following expression has been used [24]:

$$\bar{b}_\alpha^{(k)} = L_\alpha^k \frac{m^{k/3} + n^{k/3}}{(m+n)^{k/3}}. \quad (30)$$

where  $m$  and  $n$  represent the mass ratios between the two fragments. For example, if  $m=1$  and  $n=1$ , the two fragments have the same volume and thus, symmetric fragmentation is considered. If  $m \neq n$ , then fragmentation is not symmetric and a particular case is when  $m \gg n$  (or  $n \gg m$ ) which is known as erosion. In this work, two different values of  $m$  and  $n$  have been considered. Most of the simulations were run with  $m=n=1$ , but in Section 4.4, erosion is also investigated and compared with symmetric fragmentation.

The kinetic theory of granular flow can be applied to derive expressions for aggregation and breakage kernels in fluidized beds. According to this theory, the number of collisions per unit volume and time between particles with indices  $\alpha$  and  $\gamma$  is given by [32]

$$N_{\alpha\gamma} = \pi \omega_\alpha \omega_\gamma \sigma_{\alpha\gamma}^3 g_{\alpha\gamma} \left[ \frac{4}{\sigma_{\alpha\gamma}} \left( \frac{\theta_s}{\pi} \frac{m_\alpha + m_\gamma}{2m_\alpha m_\gamma} \right)^{1/2} - \frac{2}{3} (\nabla \cdot \mathbf{u}_s) \right], \quad (31)$$

where  $m_\alpha$  and  $m_\gamma$  are the masses of the particles of size  $L_\alpha$  and  $L_\gamma$ , respectively,  $\sigma_{\alpha\gamma}$  and  $\theta_s$  are the average particle size and average granular temperature of the solid mixture, respectively, and  $g_{\alpha\gamma}$  is the radial distribution for the mixture (see Table 1 for the definitions of these parameters). Thus, the aggregation kernel can be expressed as

$$\beta_{\alpha\gamma} = \Psi_a \pi \sigma_{\alpha\gamma}^3 g_{\alpha\gamma} \left[ \frac{4}{\sigma_{\alpha\gamma}} \left( \frac{\theta_s}{\pi} \frac{m_\alpha + m_\gamma}{2m_\alpha m_\gamma} \right)^{1/2} - \frac{2}{3} (\nabla \cdot \mathbf{u}_s) \right], \quad (32)$$

where  $\Psi_a$  is the success-factor for aggregation, which is usually a function of particle temperature, particle velocity and particle position. Likewise, the breakage kernel can be expressed as

$$a_\alpha^* = \Psi_b \sum_{\gamma=1}^N \frac{N_{\alpha\gamma}}{\omega_\alpha} \quad (33)$$

where  $\Psi_b$  is the success-factor for breakage. In this work, we will simply assume that  $\Psi_a$  and  $\Psi_b$  are constant.

If we neglect the divergence of the particle velocity field and assume that particles have equal density, Eq. (32) can be rewritten as

$$\beta_{\alpha\gamma} = \Psi_a g_{\alpha\gamma} \left( \frac{3\theta_s}{\rho_s} \right)^{1/2} (L_\alpha + L_\gamma)^2 \left( \frac{1}{L_\alpha^3} + \frac{1}{L_\gamma^3} \right)^{1/2}. \quad (34)$$

Likewise, Eq. (33) can be rewritten as

$$a_\alpha^* = \Psi_b \sum_{\gamma=1}^N \omega_\gamma g_{\alpha\gamma} \left( \frac{3\theta_s}{\rho_s} \right)^{1/2} (L_\alpha + L_\gamma)^2 \left( \frac{1}{L_\alpha^3} + \frac{1}{L_\gamma^3} \right)^{1/2}. \quad (35)$$

These are the kinetic-theory kernels used in the simulations reported in Section 4.

#### 4. Results and discussion

The mathematical model described above is incorporated in the multi-fluid CFD code MFIX, which is a general-purpose hydrodynamic model for describing dense or dilute gas–solids flows. The semi-implicit method for pressure linked equations (SIMPLE) scheme and automatic time-step adjustment are used to speed up the calculation. A second-order spatial discretization method is adopted to increase the accuracy of the code. Due to the strong coupling between the phases through the drag forces, the partial elimination algorithm of Spalding (PEAS) is used to handle the inter-phase coupling [33]. All of the simulations reported here were run on an Alpha Cluster made up of Compaq XP1000 workstations. The average time step  $\Delta t$  for the simulation was approximately  $3 \times 10^{-4}$  s.

Two-dimensional simulations were carried out for an FB reactor. The computational domain and solid physical properties are reported in Table 3. The initial static bed height was 15.9 cm. The gas velocity was 20 cm/s, and the density and viscosity of air at room temperature were used in the simulation. First, the code was tested with constant aggregation and breakage kernels and then by using the expressions derived from kinetic theory (Eqs. (34) and (35)). The effect of the number of nodes  $N$  has been tested and predictions with  $N=2, 3$  and 4 have been compared. The comparison was made with the same initial PSD, and thus, the initial conditions have been calculated by using the same set of moments  $m_k$  (see Table 4) for all values of  $N$ . In order to initialize the fields, starting from the first  $2N$  moments  $m_k$  ( $k=0, \dots, 2N-1$ ) the  $N$  weights  $w_\alpha$  and the  $N$  abscissas  $L_\alpha$

Table 3

The computational domain and solids physical properties in the simulation

<i>Computational domain</i>	
Width (cm)	10.1
Height (cm)	50.0
Number of grid cells	$15 \times 50$
Cell width, $\Delta_x$ (cm)	0.67
Cell height, $\Delta_y$ (cm)	1.0
<i>Particle physical properties</i>	
Particle density, $\rho_s$ (kg/m <sup>3</sup> )	2530
Coefficient of restitution, $e$	0.8
Packed bed void fraction, $\epsilon_g^*$	0.38



Table 4

Initial values of particle diameters ( $d_{pz}$ ) and solid-phase volume fractions ( $\epsilon_{sz}$ ) for  $N=2, 3$  and 4 for the same initial PSD ( $m_0=32,050.825 \text{ cm}^{-3}$ ,  $m_1=670.285 \text{ cm}^{-2}$ ,  $m_2=15.245 \text{ cm}^{-1}$ ,  $m_3=0.385$ ,  $m_4=1.09 \times 10^{-2} \text{ cm}$ ,  $m_5=3.43 \times 10^{-4} \text{ cm}^2$ ,  $m_6=1.18 \times 10^{-5} \text{ cm}^3$ ,  $m_7=4.28 \times 10^{-7} \text{ cm}^4$ )

	$N$	$\alpha=1$	$\alpha=2$	$\alpha=3$	$\alpha=4$
Particle diameter, $d_{pz}$ ( $\mu\text{m}$ )	2	183	356		
	3	174	263	409	
	4	171	225	316	420
Phase volume fraction, $\epsilon_{sz}$	2	0.274	0.356		
	3	0.196	0.229	0.205	
	4	0.157	0.157	0.157	0.157

were calculated by using the PD algorithm [22,26] and assumed to be homogeneously distributed in the initial static bed.

#### 4.1. Constant kernels

In the first set of simulations, constant aggregation and breakage kernels were used. Thus, the aggregation kernel  $\beta_{\alpha\gamma}$  and the breakage kernel  $a_\alpha$  were assumed to be independent of the particle diameter, velocity and other properties. The values of model parameters used in the simulations are listed in the Table 4. Three cases have been investigated and compared. In Case 1, the aggregation and breakage kernels are both set equal to zero. In Case 2, the aggregation kernel was set equal to  $1 \times 10^{-5} \text{ m}^3/\text{s}$ , and the breakage kernel to  $0.1 \text{ s}^{-1}$ . In Case 3, the aggregation kernel was set equal to  $1 \times 10^{-5} \text{ m}^3/\text{s}$ , and the breakage kernel to  $1 \text{ s}^{-1}$ . For future reference, note that Case 2 will be dominated by aggregation, while Case 3 will be dominated by breakage.

If no aggregation and breakage are present (Case 1), the PSD does not change with time and the volume-average mean particle size is constant. However, due to the differences in size between the  $N$  solid phases and therefore the difference in the drag force, particle segregation by size will occur. Indeed, smaller particles will tend to reside in the upper part of the bed, whereas bigger particles will tend to stay near the bottom. For Case 2, aggregation is dominant and the particles become larger and larger, so the volume-average mean particle size will increase with the time. For Case 3, breakage is dominant and the particles become smaller and smaller, and the volume-average mean particle size decreases with the time. The volume-average mean particle size in the fluidized bed for these three cases are shown in Fig. 1 for  $N=2, 3$  and 4. Note that the volume-average mean particle size reported here is  $d_{32}$ , namely the ratio between the third moment  $m_3$  and the second moment  $m_2$  of the PSD. Note that the results are nearly independent of  $N$  for constant aggregation and breakage. There are significant fluctuations for Case 3, caused by the dilute system resulting from high breakage.

As already mentioned, the DQMOM is based on a presumed functional form of the PSD that allows us to solve the closure problem and track with excellent accuracy

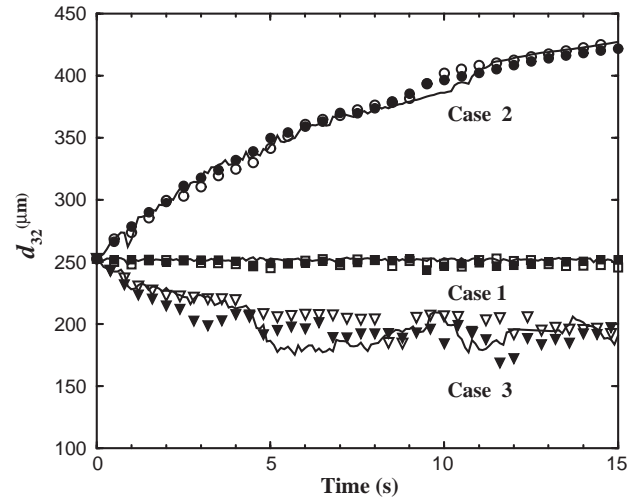


Fig. 1. Volume-average mean particle size ( $d_{32}$ ) for  $N=2$  (filled symbols),  $N=3$  (empty symbols), and  $N=4$  (lines).

the moments of the distribution. Moreover, the different delta functions are treated as distinct solid phases. Although the underlying PSD could be retrieved by a sufficiently large number of moments [19] in what follows we use a volume-fraction versus particle-size diagram to report on the position of the  $N$  delta functions. As explained in our previous work [24], this can give some insight into the shape of the underlying PSD, although the real and presumed PSDs share only a fixed set of moments.

The PSD at the middle of the FB bed for Cases 2 and 3 at selected times are shown in Figs. 2 and 3, respectively. At time zero, there are four particles with different particle sizes and the same solid void fraction for both cases. For the aggregation dominated case (Fig. 2), smaller particles aggregate and produce large particles, and the volume fraction for smaller particles decreases with time. At 15 s, a broad

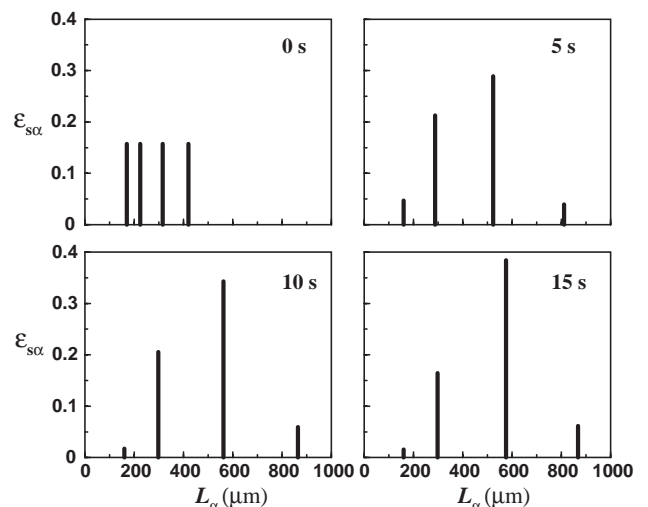


Fig. 2. PSD at the middle of the FB at 0, 5, 10 and 15 s for Case 2.



distribution of particle sizes exists in the bed. For the breakage-dominated case (Fig. 3), particles become smaller due to breakage. Indeed, more and more smaller particles are produced due to the excessive breakage. The bed becomes more dilute with the newly formed smaller particles, and the PSD changes very quickly. Thus, the PSD at different times are quite different.

As discussed in Section 1, DQMOM was developed from QMOM. By using DQMOM, we do not need to solve the transport equations for the moments. Nevertheless, information about the moments is still valuable. Comparisons of the volume-average normalized moments for Cases 2 and 3 are given in Figs. 4 and 5, respectively. The normalized moments are calculated by dividing the volume-average moments by their values at time  $t=0$ :

$$\mu_k(t) = \frac{\bar{m}_k(t)}{\bar{m}_k(0)}. \quad (36)$$

Some moments have particular physical meaning. For example,  $m_0$  represents the total particle number density, whereas  $m_2$  is related to the total particle area, and  $m_3$  is related to the total particle volume. For Case 2, it is possible to see that  $N=2, 3$  and  $4$  gives very similar predictions. In Fig. 4, the expected effects of aggregation are observed: the total particle number density ( $m_0$ ) decreases, as do  $m_1$  and  $m_2$ , whereas the total particle volume  $m_3$  remains constant.

For Case 2, strong segregation occurs in the bed while particles are aggregating. Large particles migrate to the bottom of the fluidized bed and small particles move to the top. Aggregation continues after segregation and the big particles in the bottom keep aggregating and getting larger until large regions of the bed become defluidized. This transition is shown in Figs. 6–8, where contour plots of the mean particle size  $d_{32}$  at  $t=5, 10$  and  $15$  s, using  $N=2, 3$  and  $4$  are reported. From the plots, we can see that although the mean particle size  $d_{32}$  over the whole domain is nearly

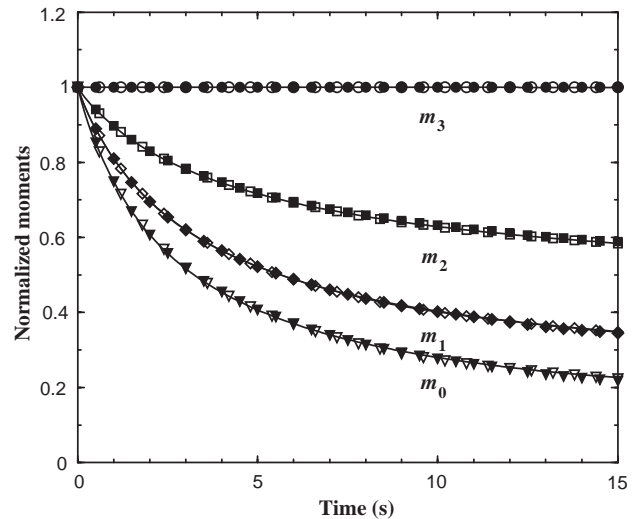


Fig. 4. Volume-average normalized moments for Case 2 using  $N=2$  (filled symbols),  $N=3$  (empty symbols), and  $N=4$  (lines).

the same for all  $N$ , the contour plots of  $d_{32}$  at different time are slightly different. The contour plots for  $N=3$  and  $4$  are more similar. Notice that because the kernels are constant for this case, even after defluidization particles continue to grow. This artifact can be eliminated by using the kinetic-theory kernels as described below.

For Case 3, it is possible to see from Fig. 5 that the evolution of the moments is opposite of Case 2 (i.e.,  $m_0, m_1$  and  $m_2$  increase). However, as before  $m_3$  remains constant, since breakage is also a volume-preserving process. In this case, some differences between  $N=2, 3$  and  $4$  are detected. The different behavior can be attributed to elutriation of the smallest particles. Because of the higher breakage rates, some very small particles are produced and depending on the gas velocity these particles can leave the bed from the

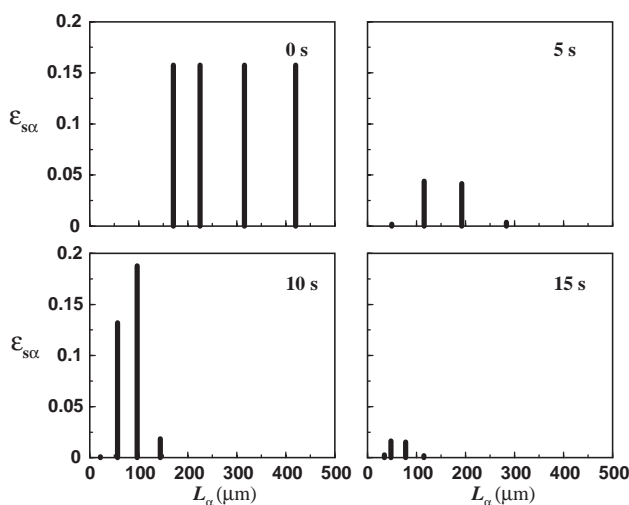


Fig. 3. PSD at the middle of the FB at 0, 5, 10 and 15 s for Case 3.

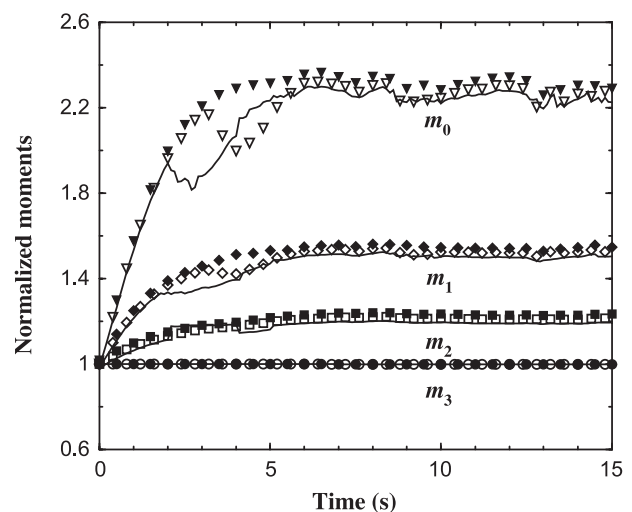


Fig. 5. Volume-average, normalized moments for Case 3 using  $N=2$  (filled symbols),  $N=3$  (empty symbols), and  $N=4$  (lines).



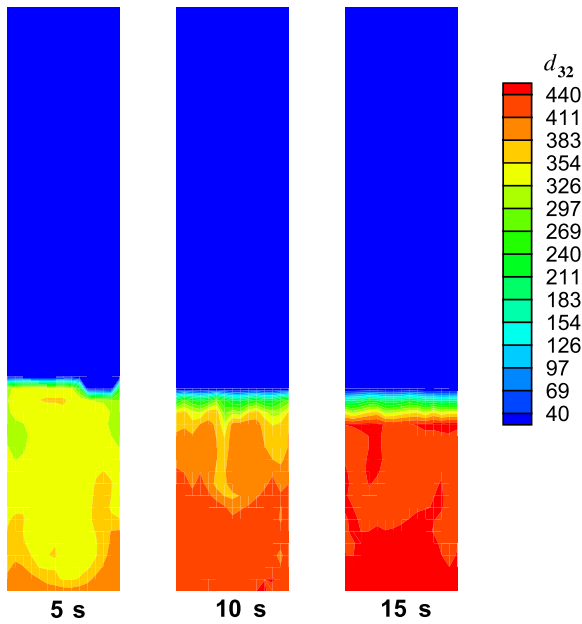


Fig. 6. Time evolution of the spatial distribution of the mean particle size ( $d_{32}$ ) for Case 2 using  $N=2$ .

top. This strongly affects the total number of particles  $m_0$ , but the effect of this loss of particles is less important for  $m_1$ ,  $m_2$  and almost negligible for  $m_3$ . In fact, because the particles leaving the domain are very small, they represent a very small fraction of the volume of the bed and thus  $m_3$  does not change appreciably. For Case 3, no defluidization is observed. In fact, due to the higher breakage rates, the volume-average mean particle size  $d_{32}$  decreases, and particles are kept well mixed by the gas flow. Because of the

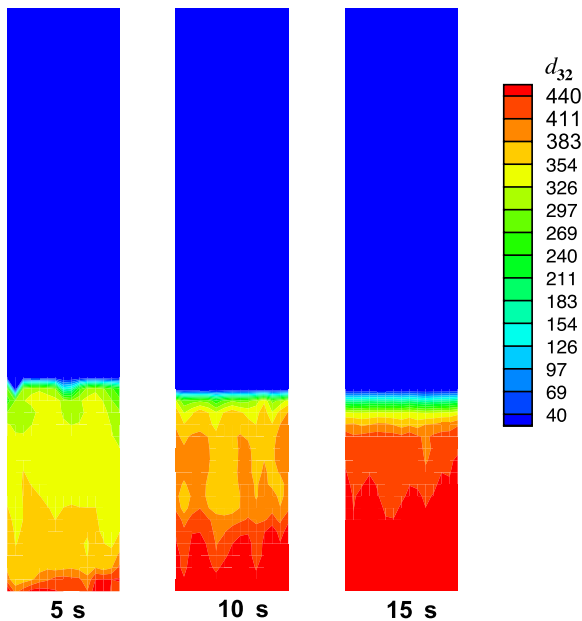


Fig. 7. Time evolution of the spatial distribution of the mean particle size ( $d_{32}$ ) for Case 2 using  $N=3$ .

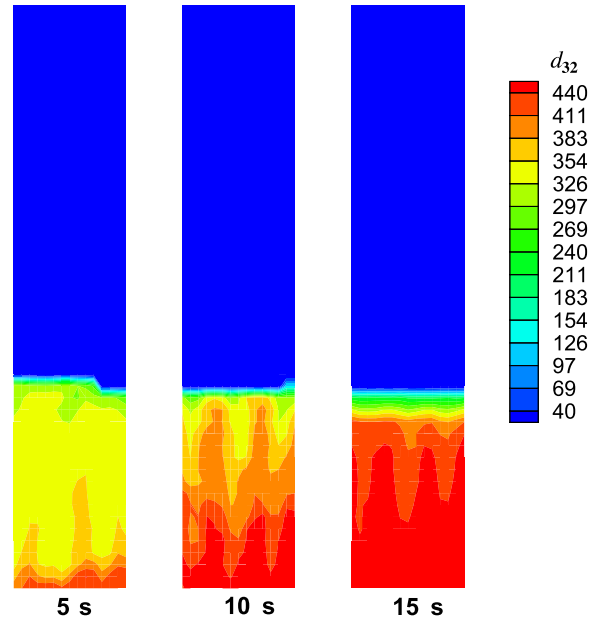


Fig. 8. Time evolution of the spatial distribution of the mean particle size ( $d_{32}$ ) for Case 2 using  $N=4$ .

reduction in the mean particle size, the bed expands and the total particle number density locally decreases, reducing the breakage rate.

Overall, from the constant-kernel cases, we can conclude that our numerical implementation of the DQMOM-multi-fluid model in MFIx works as expected. From a computational point of view, the additional CPU time needed to include DQMOM is small relative to the total CPU time needed to solve the multi-fluid model with the same value of  $N$  but without aggregation and breakage. For example, using four nodes, the additional time for calculating the source term for DQMOM is only 18%. Regarding the dependence of the results on the number of nodes used in the quadrature, we find that for the constant-kernel cases, reasonably accurate results can be obtained with only  $N=2$ . This is consistent with our earlier QMOM work [24] where it was shown that even for complicated aggregation and breakage kernels, the errors in the lower-order moments with  $N \leq 4$  are uniformly small.

#### 4.2. Kinetic-theory kernels

As noted above, constant aggregation and breakage kernels cannot represent the FB reactor realistically. This problem can be addressed by using the aggregation and breakage kernels from kinetic theory reported in Eqs. (32) and (33). Simulations have been carried out for  $N=2, 3$  and 4. The simulation conditions in Table 3 were again used for the kinetic-theory kernels. Two different cases were investigated and compared. In Case 4, the aggregation success factor  $\Psi_a$  was 0.001 and the breakage success factor  $\Psi_b$  was 0.0001. In Case 5, the success factors for aggregation and breakage had the same value: 0.001.



In Fig. 9, the volume-average mean particle size  $d_{32}$  is reported for Case 4. As it is possible to see,  $d_{32}$  increases with time. Several phenomena occur simultaneously. First, particles begin to aggregate and, due to their increased size, move to the bottom of the reactor. Particles near the bottom of the reactor continue to aggregate until defluidization occurs. At this point, the granular temperature  $\theta_s$  is null, and thus, the aggregation and breakage kernels are null. No further particle aggregation (nor breakage) can occur. Although the volume-average mean particle size predicted by using two, three and four nodes are very similar, some difference in the defluidization dynamics can be observed. Generally speaking, a higher number of nodes represents the system more accurately, but increases the computational time. For example, the CPU time required for running a simulation with  $N=4$  is 1.8 times higher than with  $N=3$ , and 3.4 times higher than with  $N=2$ .

Results for Case 5 are reported in Fig. 10. As it is possible to see, also for this case, the volume-average mean particle size predicted by the DQMOM using two, three and four nodes is very similar. From Cases 4 and 5, we note that the mean particle size distributions are nearly the same when breakage dominates or when mixing is significant. However, when segregation is significant, using different values of  $N$  produces different results. Nevertheless, as  $N$  increases, the results show closer agreement. In consideration of the computation cost, simulations with three nodes appears to be sufficient to represent the PSD.

The instantaneous contour plots for the gas void fraction at 6 s using  $N=3$  for Cases 4 and 5 are compared with Case 1 (no aggregation and breakage) in Fig. 11. It can be clearly seen that with aggregation, the fluidized bed becomes defluidized and the bed height decreases compared to no aggregation and breakage (Case 1). Due to the

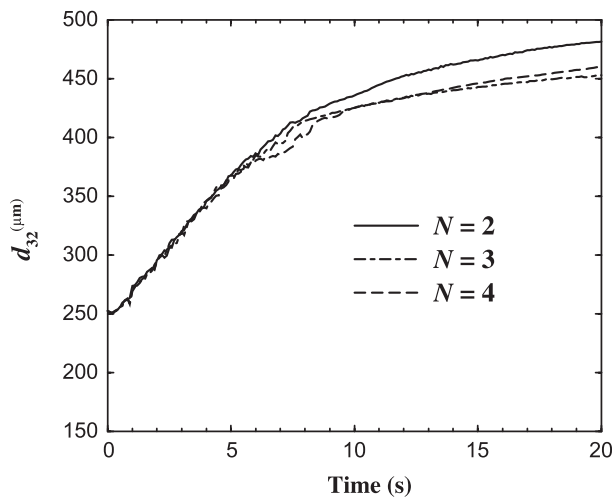


Fig. 9. Volume-average mean particle size for Case 4.

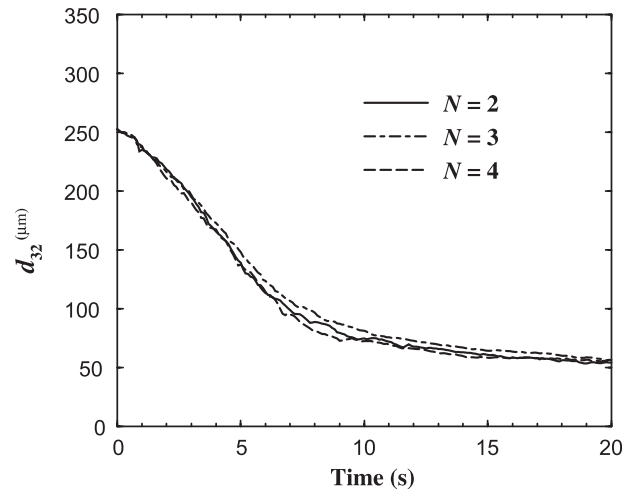


Fig. 10. Volume-average mean particle size for Case 5.

high degree of aggregation, the particles become larger and the fluidized bed becomes a packed bed. (The void fraction is near to the maximum packed void fraction.) Only a few bubbles are observed near the top of the bed. For the case dominated by breakage, the particles become smaller and remain well mixed. The bed height expands compared to Case 1, and larger bubbles are observed in the fluidized bed.

#### 4.3. Effect of the aggregation success factor

The success factor for aggregation  $\Psi_a$  is a very important parameter that affects the PSD evolution and defluidization

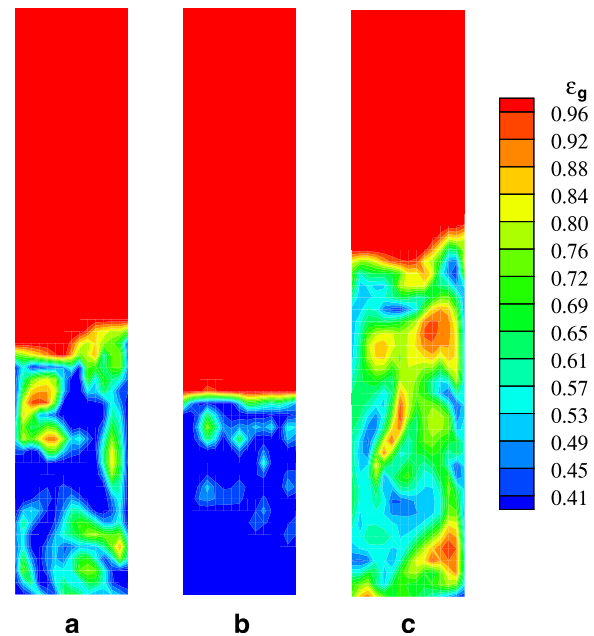


Fig. 11. Contour plots of the gas volume fraction at 6 s. (a) Case 1. (b) Case 4. (c) Case 5.



dynamics. The role of this parameter has been investigated for  $N=3$ , and three different values of the success factor  $\Psi_a=0.001$ , 0.0005 and 0.0001 were tested. In these simulations, the success factor for breakage  $\Psi_b$  was set to zero. Results are first compared in terms of the pressure-drop fluctuations in the gas–solid fluidized bed for different values of  $\Psi_a$  in Fig. 12. Notice that the pressure-drop fluctuations go to zero when the bed becomes totally defluidized. The time for defluidization using the success factors reported above is 6, 11.5 and 50 s, respectively. Results show that an increase in the success factor causes earlier defluidization of the bed. Moreover, an increase in  $\Psi_a$  causes an increase in the final mean particle size, as shown in Fig. 13.

#### 4.4. Effect of the fragment distribution function

All the simulations above have been carried out using symmetric fragmentation, but erosion can also be very important in fluidized beds. Erosion is a fragmentation process which results in the formation of a small and a big fragment, and thus, it is the separation of a small “chip” from a larger particle. Indeed, different mass ratios can be considered which still belong to the erosion-type fragmentation mechanism. In what follows the results from Case 5 (where in Eq. (30),  $m=n=1$ ) are compared with results obtained under the same operating conditions but with  $m=9$

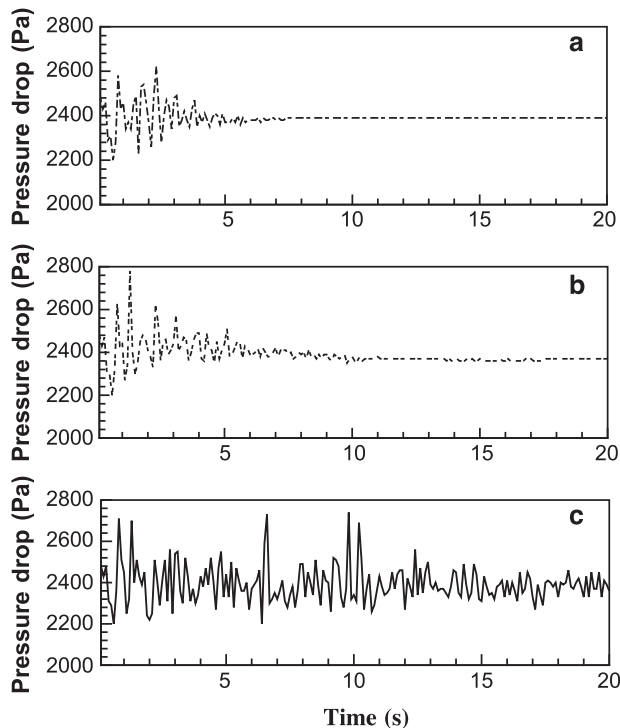


Fig. 12. Pressure drop fluctuations in gas–solid fluidized bed for three different values of the aggregation success factor. (a)  $\Psi_a=0.001$ . (b)  $\Psi_a=0.0005$ . (c)  $\Psi_a=0.0001$ . Note that the pressure fluctuations cease when the bed defluidizes.

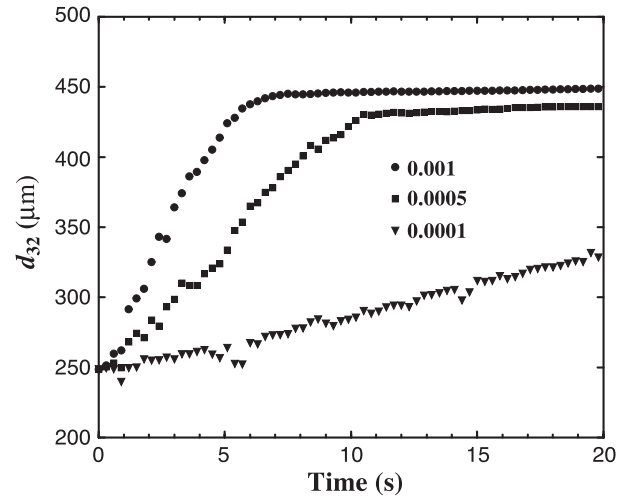


Fig. 13. Effect of the value of the aggregation success factor ( $\Psi_a$ ) on the volume-average mean particle size.

and  $n=1$  (which implies the formation of a fragment whose volume is nine times smaller than the volume of the other fragment) using  $N=3$ . Fig. 14 shows a comparison between symmetric fragmentation and erosion for the volume-average mean particle size. Results show that erosion causes a delay in the dynamic response of the mean particle size. This is due to the fact that erosion is a less effective breakage mechanism in the presence of aggregation. With symmetric fragmentation, particles reduce their volume by a factor of two, whereas with erosion a large particle generates a small fragment and a second fragment which has nearly the original volume.

It is interesting to note that with erosion, another phenomenon can occur. The small fragments generated in the erosion process become smaller at a faster rate than with

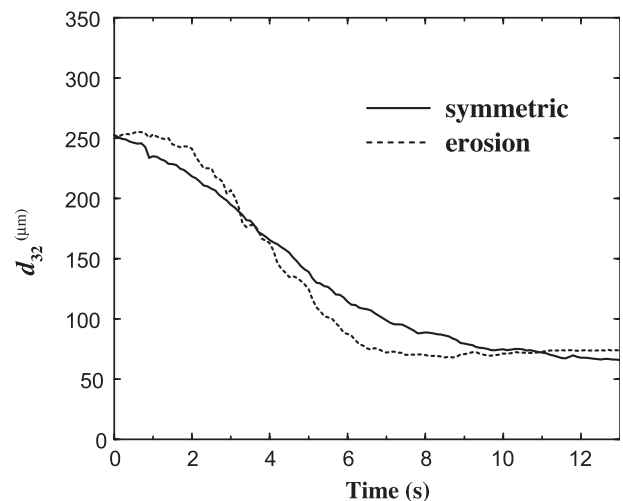


Fig. 14. Effect of symmetric fragmentation versus erosion on the volume-average mean particle size.



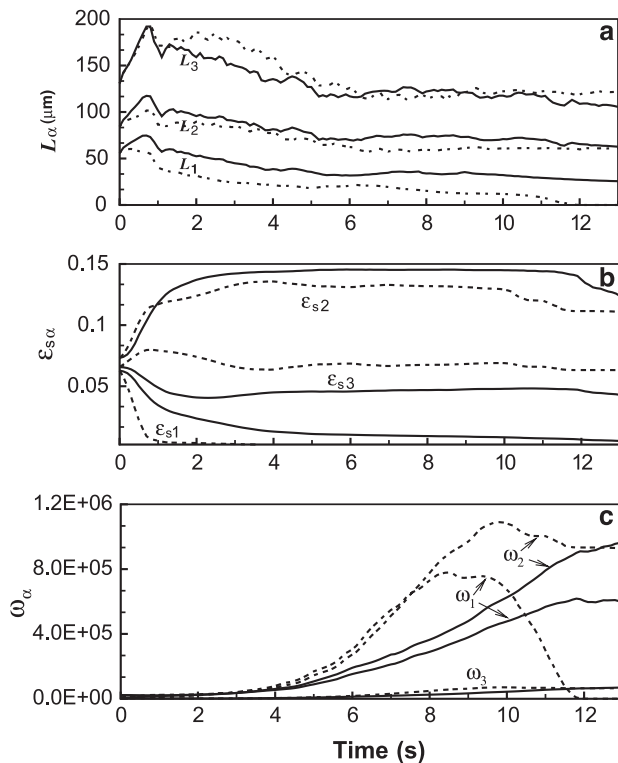


Fig. 15. Comparison between symmetric fragmentation (solid lines) and erosion (dashed lines). (a) Abscissas. (b) Solid volume fractions. (c) Weights.

symmetric fragmentation and in a finite time, an infinite number of particles with null size can be generated. This phenomenon goes under the name of shattering and can be detected by a net loss of mass. In Fig. 15, the three volume-average abscissas  $L_\alpha$ , volume fractions  $\epsilon_{s\alpha}$  and weights  $\omega_\alpha$  are reported for symmetric fragmentation and erosion. As it is possible to see, with erosion the smallest class  $L_1$  becomes null in a finite time (about 12 s) and the corresponding volume fraction  $\epsilon_{s1}$  becomes zero. The corresponding weight  $\omega_1$  should become infinite but since the equation is not directly solved for  $\omega_\alpha$ , it tends to be zero instead.

## 5. Conclusions

Simulation results show that the DQMOM-multi-fluid model is an effective approach to represent the evolution of the PSD due to aggregation and breakage in FB reactors. Two different sets of aggregation and breakage kernels were tested. For FB reactors, the kernel developed from kinetic theory should be more accurate than the constant kernel. With the kinetic-theory kernel, the mean particle size stops increasing when the fluidized bed becomes totally defluidized. Nevertheless, both kernels can describe the phenomena of particle growth, segregation, and elutriation due to aggregation and breakage. The performance of the DQMOM-multi-fluid model using two, three and four nodes

has been tested. Results show that model predictions are very similar for  $N=2-4$ . However, for some cases, using three or four nodes produces similar results, which are different from those found with two nodes. Considering the increase in computational time with an increasing number of nodes, three nodes appears to be a good choice for representing FB reactors. The effect of the success factor for aggregation  $\Psi_a$  was investigated for the kinetic-theory kernel. As expected, a high success factor  $\Psi_a$  leads to a shorter time for reaching complete defluidization.

For modeling real systems, several additional features (e.g., heat and mass transfer, chemical reactions, etc.) must be added to the CFD model proposed in this work. However, the conceptual framework of the DQMOM-multi-fluid model need not be changed to accommodate these additional features. In other work, we apply the CFD modeling approach developed in this work to FB poly-olefin reactors used to produce high-density polyethylene as well as other polymers [34]. For these reactors, the formation of hot spots can lead to aggregation of the polymer particles and eventually to reactor shutdown. For this reason, the ability to describe polydisperse, aggregating particles is a central requirement of any CFD model for FB poly-olefin reactors. The DQMOM-multi-fluid model developed here provides a computationally efficient and robust method for attaining this objective.

## Acknowledgements

This work was supported by the U.S. Department of Energy (NETL) and the U.S. National Science Foundation (CTS-0112571).

## References

- [1] V. Mathiesen, T. Solberg, B.H. Hjertager, Predictions of gas/particle flow with an Eulerian model including a realistic particle size distribution, *Powder Technol.* 112 (2000) 34.
- [2] J.Y. Kim, K.Y. Choi, Modeling of particle segregation phenomena in a gas phase fluidized bed olefin polymerization reactor, *Chem. Eng. Sci.* 56 (2001) 4069.
- [3] H. Hatzantonis, A. Goulas, C. Kiparissides, A comprehensive model for the prediction of particle-size distribution in catalyzed olefin polymerization fluidized-bed reactors, *Chem. Eng. Sci.* 53 (1998) 3251.
- [4] H. Yiannoulakis, A. Yiagopoulos, C. Kiparissides, Recent developments in the particle size distribution modeling of fluidized-bed olefin polymerization reactors, *Chem. Eng. Sci.* 56 (2001) 917.
- [5] B.G.M. van Wachem, J.C. Schouten, C.M. van den Bleek, R. Krishna, J.L. Sinclair, CFD modeling of gas-fluidized beds with a bimodal particle mixture, *AIChE J.* 47 (2001) 1292.
- [6] M.A. Howley, B.J. Glasser, Hydrodynamics of a uniform liquid-fluidized bed containing a binary mixture of particles, *Chem. Eng. Sci.* 57 (2002) 4209.
- [7] B.P.B. Hoomans, J.A.M. Kuipers, W.J. Briels, W.P.M. Van Swaaij, Discrete particle simulation of bubble and slug formation in a two-dimensional gas-fluidized bed: a hard-sphere approach, *Chem. Eng. Sci.* 51 (1996) 99.



- [8] E. Olmos, C. Gentric, Ch. Vial, G. Wild, N. Midoux, Numerical simulation of multiphase flow in bubble column reactors. Influence of bubble coalescence and break-up, *Chem. Eng. Sci.* 56 (2001) 6359.
- [9] S. Lo, Application of population balance to CFD modeling of bubbly flow via the MUSIG model, AEA Technology, AEAT-1096.
- [10] F. Lehr, D. Mewes, A transport equation for the interfacial area density applied to bubble columns, *Chem. Eng. Sci.* 56 (2001) 1159.
- [11] B.C.H. Venneker, J.J. Derksen, H.E.A. van den Akker, Population balance modeling of aerated stirred vessels based on CFD, *AIChE J.* 48 (2002) 673.
- [12] V.V. Buwa, V.V. Ranade, Dynamics of gas–liquid flow in a rectangular bubble column: experiments and single/multi-group CFD simulation, *Chem. Eng. Sci.* 57 (2002) 4715.
- [13] D. Ramakrishna, *Population Balances*, Academic Press, London, 2000.
- [14] M. Smith, T. Matsoukas, Constant-number Monte Carlo simulation of population balances, *Chem. Eng. Sci.* 53 (1998) 1777.
- [15] K. Lee, T. Matsoukas, Simultaneous coagulation and break-up using constant- $N$  Monte Carlo, *Powder Technol.* 110 (2000) 82.
- [16] L. Madec, L. Falk, E. Plasari, Simulation of agglomeration reactors via a coupled CFD/direct Monte-Carlo method, *Chem. Eng. Sci.* 56 (2001) 1731.
- [17] L. Madec, L. Falk, E. Plasari, Modelling of the agglomeration in suspension process with multidimensional kernels, *Powder Technol.* 130 (2003) 147.
- [18] H.M. Hulburt, S. Katz, Some problems in particle technology, *Chem. Eng. Sci.* 19 (1964) 555.
- [19] R.B. Diemer, J.H. Olson, A moment methodology for coagulation and breakage problems: Part 2. Moment models and distribution reconstruction, *Chem. Eng. Sci.* 57 (2002) 2211.
- [20] R. McGraw, Description of aerosol dynamics by the quadrature method of moments, *Aerosol Sci. Technol.* 27 (1997) 255.
- [21] H. Dette, W.J. Studden, *The Theory of Canonical Moments with Applications in Statistics, Probability and Analysis*, Wiley, New York, 1997.
- [22] R.G. Gordon, Error bounds in equilibrium statistical mechanics, *J. Math. Phys.* 9 (1968) 655.
- [23] J.C. Barret, N.A. Webb, A comparison of some approximate methods for solving the aerosol general dynamic equation, *J. Aerosol Sci.* 29 (1998) 31.
- [24] D.L. Marchisio, R.D. Vigil, R.O. Fox, Quadrature method of moments for aggregation-breakage processes, *J. Colloid Interface Sci.* 258 (2003) 322.
- [25] D.L. Marchisio, J.T. Piktura, R.O. Fox, R.D. Vigil, A.A. Barresi, Quadrature method of moments for population-balance equations, *AIChE J.* 49 (2003) 1266.
- [26] D.L. Marchisio and R.O. Fox, Direct quadrature method of moments: derivation, analysis and applications, *J. Comput. Phys.* submitted for publication.
- [27] M. Syamlal, W. Rogers, T.J. O'Brien, *MFIX Documentation: Theory Guide*, U.S. Department of Energy, Morgantown, WV, 1993.
- [28] D. Gidaspow, *Multiphase Flow and Fluidization*, Academic Press, Boston, 1994.
- [29] C.K.K. Lun, S.B. Savage, D.J. Jeffrey, N. Chepurmy, Kinetic theories for granular flow: inelastic particles in Couette flow and slightly inelastic particles in a general flowfield, *J. Fluid Mech.* 223 (1984) 140.
- [30] L.S. Fan, C. Zhu, *Principles of Gas–Solid Flows*, Cambridge Univ. Press, New York, 1998.
- [31] B.O. Arnason, J.T. Willits, Thermal diffusion in binary mixtures of smooth, nearly elastic spheres with and without gravity, *Phys. Fluids* 10 (1998) 1324.
- [32] M. Goldschmidt, *Hydrodynamic Modeling of Fluidized Bed Spray Granulation*, PhD Thesis, Twente University, The Netherlands, (2001).
- [33] M. Syamlal, *MFIX Documentation Numerical Technique*, U.S. Department of Energy, Morgantown, WV, 1998.
- [34] R. Fan, D.L. Marchisio, R.O. Fox, CFD simulation of polydisperse fluidized bed polymerization reactors, *AIChE Symposium Series*, 2003, submitted.